Arabian Journal of Chemistry (2023) 16, 105081

King Saud University

Arabian Journal of Chemistry

www.ksu.edu.sa
www.sciencedirect.com

ORIGINAL ARTICLE

Novel 2D/2D S-scheme Ni doped SnS_2/BiOBr heterostructures with enhanced photocatalytic activity

Qiang Li [a,b,*], **Lijie Wang** [a], **Jupu Song** [a], **Yajing Huang** [a], **Guoyu Xie** [a], **Yi Liu** [a], **Hong Li** [a]

[a] *Anhui Province Key Laboratory of Pollutant Sensitive Materials and Environmental Remediation, College of Physics and Electronic Information, Huaibei Normal University, Huaibei 235000, PR China*
[b] *Anhui Province Industrial Generic Technology Research Center for Alumics Materials, Huaibei Normal University, Huaibei, Anhui 235000, PR China*

Received 10 April 2023; accepted 10 June 2023
Available online 16 June 2023

KEYWORDS

BiOBr;
Ni doped SnS_2;
S-scheme;
2D/2D photocatalyst;
Pollutants degradation

Abstract Herein, novel S-scheme heterojunction of Ni doped SnS_2 (Ni-SnS_2)/BiOBr (NSB) with 2D/2D structures was fabricated by a solvothermal-precipitation route, where 2D BiOBr nanoflakes were intimately deposited on the 2D Ni-SnS_2 nanosheets surface. The obtained 2D/2D NSB composite presented largely boosted photocatalytic performances for tetracycline hydrochloride (TC) and dye decomposition compared to single catalyst. The optimized 20% Ni-SnS_2/BiOBr (NSB-20) displayed the largest rate constant (0.0488 min^{-1}), which was ca. 2.07 and 44.36 folds those of pure BiOBr and Ni-SnS_2, respectively. In addition, it possessed good stability. The improved activity could be ascribed to excellent optical response, high contact areas and 2D/2D S-scheme heterostructures, which expedited efficiently separation and transfer of photocarriers. Furthermore, the effect of some factors on TC degradation was examined and possible degradation routes of TC were proposed. Finally, S-scheme charge transfer mechanism for NSB composite was put forward on the basis of band structure analysis, electron spin resonance (ESR), in situ XPS along with DFT calculations. This investigation contributes to exploit S-scheme 2D/2D materials for environmental remediation.

---

* Corresponding author.
E-mail address: qiangli@chnu.edu.cn (Q. Li).

Peer review under responsibility of King Saud University.

ELSEVIER Production and hosting by Elsevier

https://doi.org/10.1016/j.arabjc.2023.105081

1. Introduction

In recent years, immoderate discharge of various antibiotics and organic dyes in water has brought about huge threat to the human health and ecosystem (Jia, X. et al., 2020; Liu, P. et al., 2021; Song, S. et al., 2020). To eliminate these pollutants from aquatic environment, a multitude of treatment processes have been utilized, such as physical adsorption (Li, Q. et al., 2017), biological treatment (Wiśniewska, M. et al., 2021), combustion (He, C. et al., 2023) and electrochemical oxidation (Cotillas, S. et al., 2018). Among them, semiconductor-based photocatalysis process has been regarded as one of the most powerful technologies to degrade contaminants owing to its advantages of easy operation, low cost, environmentally friendly and high efficiency (Hasanvandian, F. et al., 2022; Hasanvandian, F. et al., 2022; Zhang, B. et al., 2021; Zhang, C. et al., 2022). During the last decades, some popular photoactive materials, for example, TiO_2 and ZnO have attracted extensive attention due to their various advantages including strong oxidation ability, good stability and low cost (Shanmugaratnam, S. et al., 2021; Wang, Z. et al., 2019). Nevertheless, the photoactivities were greatly restricted by some defects such as wide band gap. To take full advantage of natural sunlight, exploring novel and efficient visible light (VL) responsive catalyst has become the hotspots of research (Zhang, B. et al., 2021). Until now, numerous visible-light-response photocatalysts, such as In_2S_3 (Murugalakshmi, M. et al., 2022), Bi_2MoO_6 (Li, M. et al., 2020), BiOI (Yang, J. et al., 2021) etc., have been developed and applied in photocatalytic reactions.

Among them, Bismuth oxyhalides (BiOBr) with special 2D layered structure has become one of the most studied photocatalytic materials because of its remarkable advantages, like moderate bandgap (~2.7 eV), non-toxicity, easy preparation, and reliable stability (Sin, J.-C. et al., 2021; Tang, Q.Y. et al., 2021; Zhao, W. et al., 2021). BiOBr has been extensively employed as photocatalyst for H_2 production (Chang, C.-J. et al., 2022), CO_2 photoreduction (Meng, J. et al., 2022; Zhou C et al., 2021), as well as organic pollutants degradation (Zhang et al., 2021). Unfortunately, single BiOBr showed low degradation efficiency because of low VL utilization and severe recombination of photocarriers (Senasu, T. et al., 2021; Wu, Y. et al., 2022). To surmount these problems, researchers have investigated various strategies, such as facet engineering (Meng, J. et al., 2022), element doping (Lv, X. et al., 2020; Wu, Y. et al., 2022), and heterojunction formation (Liang, L. et al., 2020; Ling, Y.L. et al., 2020; Ni, J. et al., 2021). Among all, building BiOBr-based S-scheme heterojunction has taken as an attractive way for improving its photocatalytic efficiency (Dou, X. et al., 2022; Dou, X. et al., 2022; Zhang, T. et al., 2021). Generally, the S-scheme system is mainly constituted by a reduction photocatalyst and an oxidation photocatalyst with staggered band structures (Zhang, X. et al., 2022). After contacting in the dark, the electrons from the reduction catalyst migrate to the oxidation catalyst across the interface, leading to the formation of an internal electric field (IEF) at the hetero-interface (Zhang, Y. et al., 2022). Driven by the IEF, the high-energetic photoinduced charge carriers with strong redox ability are effectually segregated and preserved for redox reactions (Li, S. et al., 2023). Thus, the S-scheme photocatalytic system can display preferable photocatalytic activity. Very recently, a few S-scheme composite catalysts with excellent photocatalytic behaviors have been synthesized and reported (Li, S. et al., 2022; Shao, B. et al., 2022; Su, Y. et al., 2022). For instance, the novel S-scheme $TiO_2/CsPbBr_3$ was got by electrostatic-driven self-assembling way, which displayed an enhanced activity toward CO_2 photoreduction under VL illumination (Xu, F. et al., 2020). Zhang and coworkers have prepared S-scheme WO_3/BiOBr hybrid photocatalyst enriched with oxygen vacancy, which displayed raised photocatalytic efficiency (Zhang, X. et al., 2022).

As we all know, the photocatalytic property of catalyst was closely related with its microstructures, and the construction of 2D/2D heterostructures system was believed a promising tactic in efficiently strengthening photocatalytic efficiency since it can increase contact interface area, shorten transmission distance of charge, and facilitate charge transfer and separation (Li, Y. et al., 2021; Yang, H. et al., 2019). To date, there were lots of investigations focused on 2D/2D heterojunction with preferable photocatalytic property (Li, Y. et al., 2021; Shao, B. et al., 2021; Wang W et al., 2021). For example, Fan and his group reported that 2D/2D BiOBr/g-C_3N_4 heterostructures synthesized by in situ self-assembly route exhibited outstanding activity in dyes degradation and H_2 production (Zhang, B. et al., 2021). SnS_2, a typical CdI_2-type 2D material with a relatively narrow bandgap (2.1–2.3 eV), possesses wide visible light absorption and good chemical stability (Yin, S. et al., 2021; Zai, J. et al., 2021), which makes it a promising visible light-active candidate for the pollutants degradation (Zhou, J. et al., 2020), Cr(VI) reduction (Zhao, W. et al., 2021) and water splitting (Zhao, W. et al., 2021). Hence, SnS_2 has been introduced to the photocatalysis system to enhance photocatalytic activity both for hydrogen generation and pollutant removal (Liu, E. et al., 2018; Liu, H. et al., 2018). Besides, the energy levels of SnS_2 matched well with those of BiOBr, which plays a cooperative role in the excitons dissociation. Some previous investigations have combined BiOBr with SnS_2 forming SnS_2/BiOBr and SnS_2/RGO/BiOBr to achieve higher photocatalytic efficiencies (Qiu, F. et al., 2017; Zhang, R. et al., 2021). In addition, it is suggested that reduced band gap, enhanced light absorption and boosted photocatalytic performance was achieved when Sn^{4+} was replaced by Ni^{2+} in Ni-doped SnS_2 (Ni-SnS_2) (Chen, D. et al., 2019). It would be very interesting and meaningful to fabricate 2D/2D Ni-SnS_2/BiOBr S-scheme heterojunction for water treatment. However, there is little report that has adopted Ni-doped SnS_2 to form heterojunctions with BiOBr for photocatalytic reaction until now.

Motivated by the above studies, for the first time, we designed and fabricated the S-scheme 2D/2D Ni-SnS_2/BiOBr (NSB) heterojunction via *in-situ* growth of BiOBr nanoflakes on the Ni-SnS_2 microspheres surface. The physical–chemical and optical-electrical property of the composite materials was researched through multiple characterization techniques. The 2D/2D NSB had higher surface area, abundant active sites, and improved optical-harvesting capability. Thereby, the S-scheme NSB composite presented dramatically improved photocatalytic performance and stability in decontamination of Tetracycline (TC) and Rhodamine B (RhB) under VL illumination with respect to single catalyst. Furthermore, the S-scheme photocatalytic mechanism and the generation of active species were explored and analyzed.

2. Experimental

2.1. Fabrication of Ni-SnS_2 microspheres

The Ni-SnS_2 microspheres were fabricated via a one-pot solvothermal route (Chen, D. et al., 2019). Specifically, 2 mmol of $SnCl_4·5H_2O$ and 4 mmol L-cysteine was dispersed in 60 mL of distilled water (DW) under stirring for 30 min. Then, 800 μL of 0.05 M $NiCl_2·6H_2O$ solution was added dropwise into the above solution. After stirring for 30 min, the solution was sustained at 160℃ for 24 h in a 100 mL stainless steel autoclave. Subsequently, the resulting products were washed with DW and ethanol four times, and then dried at 333 K for 12 h in a vacuum oven. The sample of pristine SnS_2 was fabricated via a similar method, but without addition of $NiCl_2·6H_2O$ solution.

2.2. Preparation of 2D/2D Ni-SnS_2/BiOBr composites

The 2D/2D Ni-SnS_2/BiOBr nanohybrids were synthesized through an in-situ precipitation route. Specifically, the as-prepared Ni-SnS_2 microspheres were added into 10 mL DW and ultrasonically dispersed for 30 min to form solution A.

Meanwhile, 4 mmol KBr was dissolved in 20 mL ethylene glycol, which was then slowly added to solution A with magnetic stirring. Then 20 mL ethylene glycol containing 4 mmol Bi $(NO_3)_3$ṡ$5H_2O$ was dispersed into the mixed solution under stirring for 3 h. After this stage, the resulting product was centrifuged, washed and dried under vacuum at 333 K for 12 h. The Ni-SnS_2/BiOBr (named as NSB) composites with different mass percentage of Ni-SnS_2 were prepared by adding various weight of Ni-SnS_2 (0.1355, 0.3048 and 0.5227 g). The corresponding photocatalysts were designated as NSB-10, NSB-20 and NSB-30, respectively. For comparison, the SB-20 (undoped Ni catalysts) sample containing 20 wt% SnS_2 and 80% BiOBr was also prepared as aforementioned route. The preparation process of 2D/2D NSB was depicted in Scheme 1.

2.3. Characterization, photocatalytic measurements and calculations

Detailed information on characterization, photocatalytic performance tests and density functional theory (DFT) calculations can be found in the supporting information.

3. Results and discussion

3.1. Structure and phase study

XRD patterns were depicted in Fig. 1a to uncover the phase and crystallographic structures of the samples. The diffraction peaks of SnS_2 were agreed with a hexagonal SnS_2 (JCPDS No. 23–0677) (Chen, D. et al., 2019). The four noticeable peaks at 15.0°, 28.2°, 32.1° and 50.0° may correspond to the (0 0 1), (1 0 0), (1 0 1) and (1 1 0) planes of hexagonal SnS_2, respectively. The as-synthesized Ni-SnS_2 showed the same XRD patterns to the SnS_2, suggesting the doping of Ni^{2+} has no effect on the crystallographic structure of the SnS2. The diffraction peaks of single BiOBr were in line with the tetragonal BiOBr phase (JCPDS No. 09–0393) (Miao, Z. et al., 2022). As expected, the diffraction peaks belonged to both Ni-SnS_2 and BiOBr was detected in the NSB nanohybrids. With the increase of Ni-SnS_2 content, the diffraction peaks intensity assigned to Ni-SnS_2 increased, while the corresponding peak intensity of BiOBr become weaker. These results revealed their coexistence and the retained crystal structure in the composite samples. Moreover, no impurity peak was detected in the composite materials, suggesting their high purity.

In order to determine the functional groups of the samples, the Fourier transform infrared (FTIR) spectroscopy was conducted. In Fig. 1b, Ni-SnS_2 and SnS_2 samples presented very similar profiles, indicating that Ni doping did not change the chemical structure of SnS_2. The two peaks were observed at 3418.5 and 1622.1 cm^{-1}, which were assigned to stretching vibration of the O–H bond (Arunkumar, M. et al., 2021). The peak located at 2934.6 cm^{-1} was associated with stretching vibrations of C–H in CH_2 (Chen, D. et al., 2019). In addition, the characteristic peaks located at 512 and 870.3 cm^{-1} were attributed to the stretching vibration of Bi-O (Wang, X. et al., 2021; Zhang, X. et al., 2022), while the absorption bands at 1389.38 cm^{-1} arose from the vibration of Bi-Br (Wu, Y. et al., 2022). All NSB samples had a similar spectrum to that of BiOBr, and the characteristic peak for Sn-S appeared at 655.2 cm^{-1} (Arunkumar, M. et al., 2021).

To study the morphological and microstructural features of the as-prepared composites, the NSB-20 that presented the highest photoactivity was selected for SEM and TEM (HRTEM) characterizations. For comparison, single-phase catalyst was also researched by SEM. Obviously, Ni-SnS_2 (Fig. 2a) presented uniform flower-like microspheres structures with size of 2–3 μm, which were composed of many interleaving nanosheets. The special 3D structures can not only improve optical absorption but also supply abundant catalytic active sites for photocatalysis reaction, thereby conducive to upgrade photocatalytic performance (Zhang, L. et al., 2020; Zhao, W. et al., 2021). Fig. 2b shows the aggregation morphology of irregular BiOBr nanoflakes with a size of about 200–300 nm. The morphology of NSB-20 hybrid material was displayed in Fig. 2c-d. Obviously, numerous BiOBr nanosheets were uniformly immobilized on the surface of Ni-SnS_2 microspheres after the synthesis process, leading to the formation of a unique hierarchical structure. TEM and HRTEM images were used to further study the morphology and structure of the as-synthesized material (Fig. 3a-3b). Fig. 3a discloses that masses of untrasmall BiOBr nanosheets with diameters of ~ 8 nm were evenly dispersed on the Ni-SnS_2 surface. It can be deduced that BiOBr nanosheets were anchored on the Ni-SnS_2 surface during precipitation process, which leads to the successful construction of NSB-20 heterostructures. HRTEM images in Fig. 3b displayed the lattice stripe spacing of 0.308 and 0.336 nm was in line with the (1 1 0) plane of Ni-SnS_2 and (0 1 1) plane of BiOBr, respectively, well agreeing with the XRD analysis. Moreover, there was a clear intimate contact interface between BiOBr and Ni-SnS_2 (Fig. 3b), which

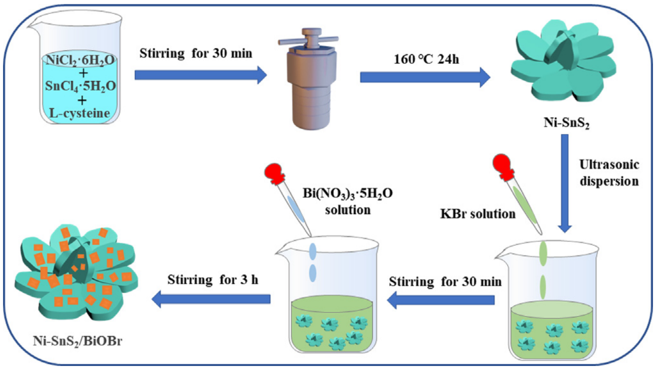

Scheme 1 Schematic diagram of the formation process of NSB composite.

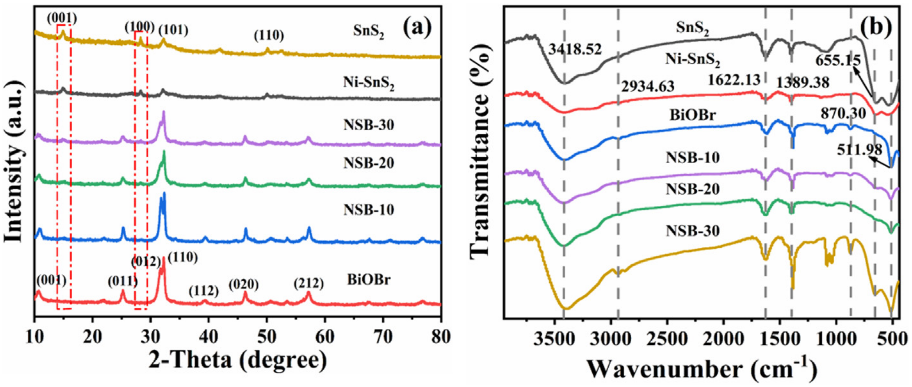

Fig. 1 (a) X-ray diffraction patterns and (b) FTIR spectra of SnS$_2$, Ni-SnS$_2$, BiOBr and NSB composites.

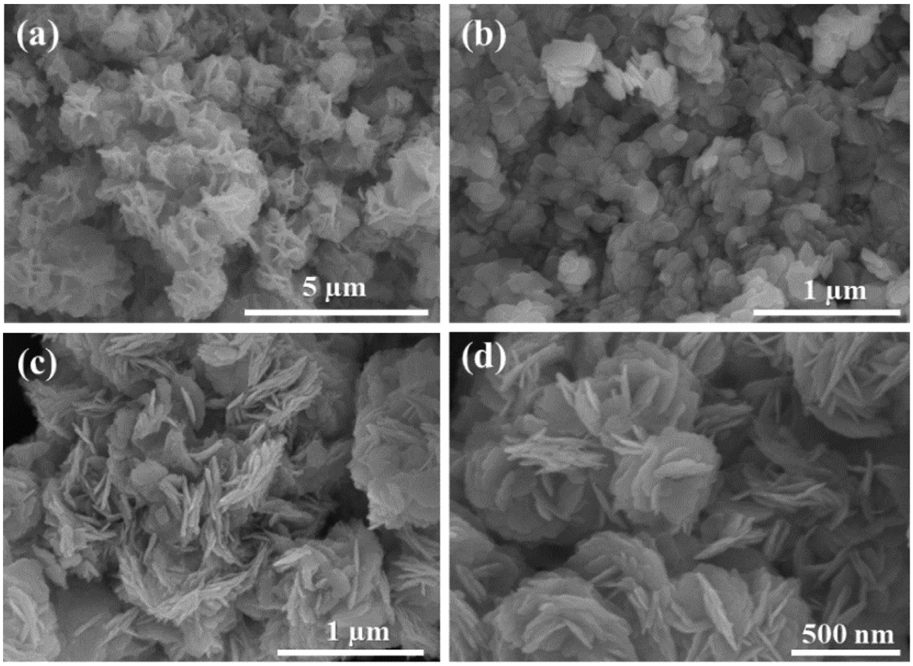

Fig. 2 SEM images of (a) Ni-SnS$_2$, (b) BiOBr and (c, d) NSB-20 composite.

was conducive to charge carriers transmission between Ni-SnS$_2$ and BiOBr. Additionally, the EDS elemental mapping clearly illustrated that the Ni, Sn, S, Bi, O and Br elements homogeneously distributed in the NSB-20 composite (Fig. 3-c-h), which also supports the fact that the successful introduction of elemental Ni. All these outcomes affirm the successful construction of 2D/2D NSB-20 heterojunction.

XPS tests were applied to further research the chemical composition and states of Ni-SnS$_2$, BiOBr, and NSB-20 photocatalyst (Fig. 4). The survey scan XPS spectra (Fig. S1) of NSB-20 displayed the presence of Ni, Sn, S, Bi, O, and Br elements, suggesting Ni-SnS$_2$ and BiOBr were successfully combined. As displayed in the Ni 2p spectrum (Fig. 4a), the characteristic peaks at 874.38 eV and 871.96 eV represented the existence of Ni^{2+} (Chen, D. et al., 2019; Thangasamy, P. et al., 2017), indicating the Ni^{2+} was successfully doped into the Sn^{4+} sites of SnS$_2$, consistent with previous study. Fig. 4b depicts double peaks at 486.45 and 494.89 eV for Ni-SnS$_2$ corresponded to Sn 3d$_{5/2}$ and Sn 3d$_{3/2}$, respectively (Kumar, G. et al., 2022; Zhao, W. et al., 2021), which implied the existence of Sn^{4+} in the Ni-SnS$_2$. S 2p XPS spectrum (Fig. 4c) of Ni-SnS$_2$ presents double peaks at 160.94 and 162.11 eV, agreeing with S^{2-} in the Ni-SnS$_2$ (Li, W. et al., 2021; Zhang, F. et al., 2021). With respect to that of SnS$_2$, the binding energy of NSB-20 on S 2p and Sn 3d increased slightly. In Fig. 4d, the O 1 s spectrum of BiOBr can be deconvoluted into three peaks at 530.67, 531.58 and 532.64 eV. The peak at 530.67 eV was relates with Bi-O bonds, while the peaks centered at 531.58 and 532.64 eV matched with the chemisorbed oxygen species (Miao, Z. et al., 2022; Zhang, X. et al., 2022; Zheng, H. et al., 2022). As shown in Fig. 4e, the Bi 4f peaks located at 159.49 and 164.79 eV correspond to Bi 4f$_{7/2}$ and Bi 4f$_{5/2}$ of Bi^{3+}, respectively (Chen, N. et al., 2022; Liu, Y. et al., 2022; Miao, Z. et al., 2022). Fig. 4f displays the XPS of Br 3d, double characteristic peaks at 68.53 and 69.51 eV were indexed to the binding energy of Br 3d in BiOBr (Chang, C.-J. et al., 2022; Du, C. et al., 2022; Liu, Y. et al., 2022). The XPS peaks of both Br and Bi in NSB-20 showed

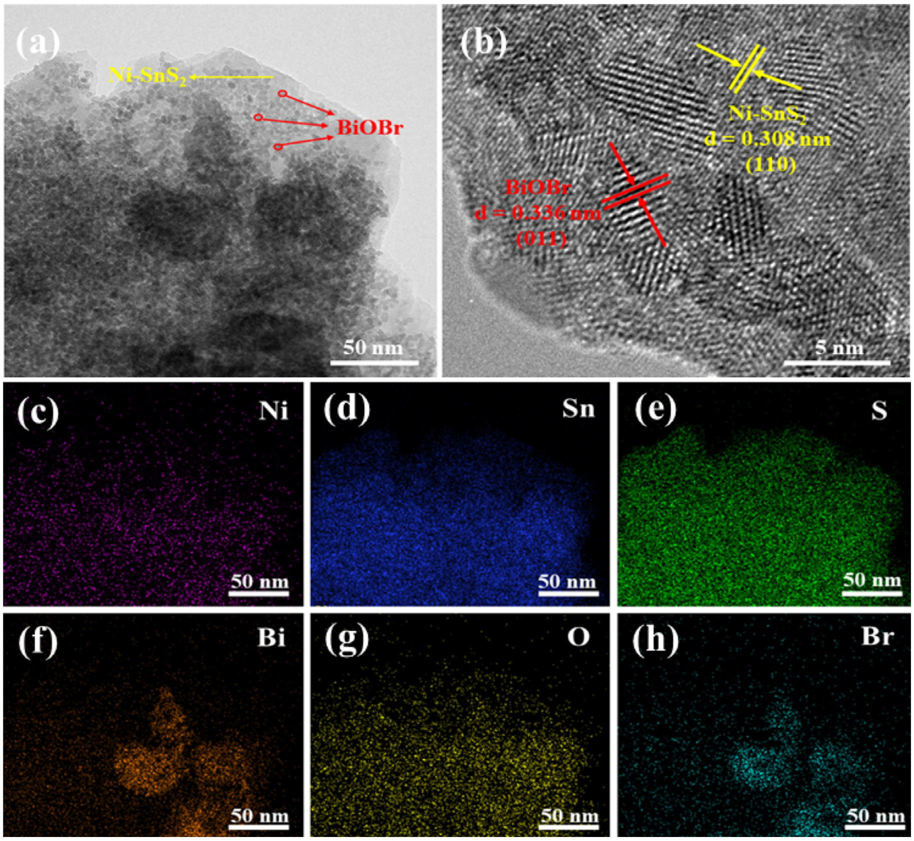

Fig. 3 (a) TEM image, (b) HRTEM image and corresponding elemental analyses: (c) Ni, (d) Sn, (e) S, (f) Bi, (g) O and (h) Br of NSB-20 composite.

a minor shift to lower energies in contrast to those in the single BiOBr. Overall, all of these peaks shifted indicate that there might be strong chemical interaction between BiOBr and Ni-SnS_2 (Ni, J. et al., 2021; Sin, J.-C. et al., 2021; Zhang, X. et al., 2022).

The UV–vis DRS were collected to reveal optical absorption ability of catalysts and displayed in Fig. 5a. The Ni-SnS_2 sample exhibited enhanced optical absorption compared with bare SnS_2 in the VL region, implying Ni doping can increase light reaping, which is conducive to boost photocatalytic performance. The absorption edge of BiOBr was about 450 nm, which agreed well with the previous report (Yu, H. et al., 2021). As expected, the optical absorption of the composite became stronger in comparison with pristine BiOBr in the whole range of 250–800 nm, suggesting loading of Ni-SnS_2 can largely enhance light absorption of BiOBr, which is of great promise to be efficient VL-driven catalysts. The band gaps (E_g) of SnS_2, Ni-SnS_2 and BiOBr were calculated as 2.03, 1.89 and 2.72 eV, respectively, based on the Tauc plot (Fig. 5b). For determining the conduction band potential (E_{CB}) of samples, the flat band (E_{fb}) potential of Ni-SnS_2 and BiOBr was researched by Mott-Schottky (MS) plots (Chen, C. et al., 2021; Senasu, T. et al., 2021). The positive slope of the MS curves denoted that both Ni-SnS_2 and BiOBr were n-type semiconductors (Fig. 5c). In addition, the E_{fb} potentials of Ni-SnS_2 and BiOBr were ca. -0.97 and -0.24 V vs. Ag/AgCl, respectively. A potential conversion between Ag/AgCl and NHE was given by $E_{NHE} = E_{Ag/AgCl} + 0.197$ (Li, S. et al., 2022). Hence, the E_{fb} potentials of Ni-SnS_2 and BiOBr were computed as -0.77 and -0.04 V vs. NHE, respectively. The E_{CB} of n-type semiconductor was ca. 0.1 V higher than the E_{fb} (Li, S. et al., 2022). Therefore, the E_{CB} of Ni-SnS_2 and BiOBr were computed as -0.87 and -0.14 V vs. NHE, respectively. Then, the valence band (E_{VB}) of samples can be determined by the formula: $E_{VB} = E_{CB} + E_g$. Hence, the E_{VB} of Ni-SnS_2 and BiOBr were calculated as 1.02 and 2.58 V vs. NHE, respectively. Thereupon, the band positions of the catalysts are obtained and displayed in Fig. 5d. Obviously, Ni-SnS_2 and BiOBr possess staggered band structure, which is a prerequisite for the construction of S-scheme heterojunction.

3.2. Photocatalytic property

The photoactivity of catalyst was appraised via decomposition of TC and RhB under VL irradiation. Prior to irradiation, catalyst and the pollutant solutions were fully blended with stirred magnetically 60 min in darkness to achieve adsorption–desorption equilibrium. From the Fig. S2, it can be seen that the NSB composites presented superior adsorption property in comparison with single catalyst, and NSB-20 owned the strongest adsorption ability, which could be due to the highest specific area of NSB-20 (Fig. S5). Furthermore, the concentrations of both TC and RhB solution was not changed after 30 min, implying that the influence of adsorption on the

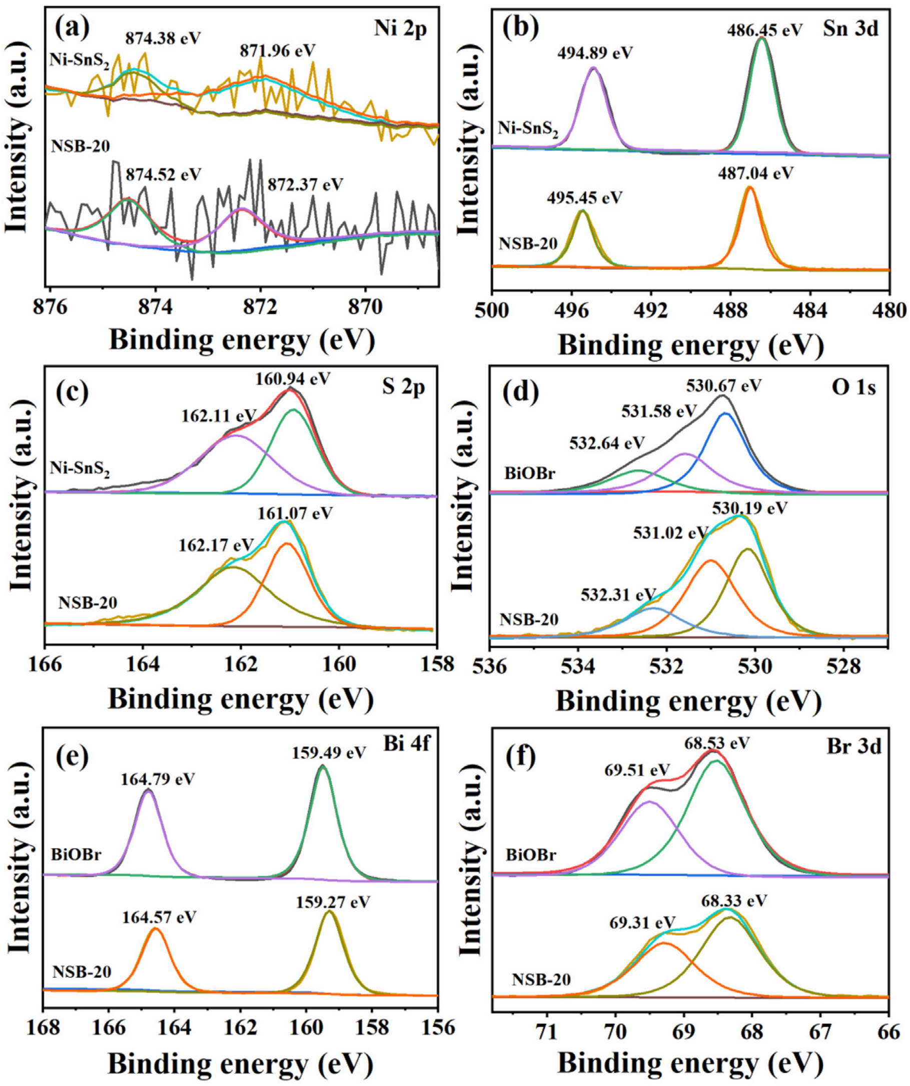

Fig. 4 High-resolution XPS spectra of (a) Ni 2p, (b) Sn 3d, (c) S 2p, (d) O 1 s, (e) Bi 4f and (f) Br 3d.

photodegradation reactions was ignorable. Fig. 6(a) depicts the degradation of TC over the as-prepared samples under irradiation of visible light. The blank tests suggested that photolysis of TC can be ignored. Single SnS$_2$ exhibited poor photodegradation capability for TC due to the strong recombination of photocarriers, whereas Ni-SnS$_2$ could degrade TC relatively quickly, suggesting that the introduction of Ni ions can boost the activity of SnS$_2$. Pristine BiOBr displayed not ideal photoactivity. Inspiringly, these NSB hybrid materials all presented higher photodegradation ability against TC (83.60% for NSB-10, 96.18% for NSB-20, and 91.99% NSB-30) than single BiOBr (75.77%), Ni-SnS$_2$ (7.6%) and the physical mixture (42.3%). The improvement of photoactivity could be due to the successful construction of 2D/2D NSB S-scheme heterojunction. Very impressively, the best-performing photocatalysts was NSB-20, indicating that the Ni-SnS$_2$ content in composites had a significant influence on their photocatalytic behaviors. Notably, the photodegradation capacity of NSB-20 was higher than that of SB-20 (86.4% degradation efficiency), highlighting the vital role of Ni ions in enhancing the photoactivity of catalysts (Chen, D. et al., 2019). Fig. S3 depicts the UV–vis absorption spectra of TC over NSB-20 composite. The main absorption peak decreased largely with time prolonging, implying TC molecules were quickly degraded by NSB-20. Besides, the mineralization efficiency of TC by NSB-20 nanohybrid was researched via total organic carbon (TOC) analysis. Fig. S4 presents that the mineralization efficiency of TC reached 82.85% after 120 min, indicating NSB-20 can effectively mineralize TC. The reaction kinetic of TC decomposition was researched through pseudo-first order kinetic model $-\ln(C_t/C_0) = kt$, where k, t, C_t, and C_0 denote the rate constant, radiation time, the concentration of pollutants at times t and 0 min, respectively (Hayati, F. et al., 2022; He, S. et al., 2021). Fig. 6b shows that the rate constant of 2D/2D NSB-20 was 0.0488 min^{-1}, which runs up to 44.36 and 2. 07 times as much as than those of 2D Ni-SnS$_2$ (0.0011 min^{-1}) and 2D BiOBr (0.0235 min^{-1}), respectively. When the content of Ni-SnS$_2$ rose from 20% to 30%, the k values declined from 0.0488 min^{-1} to 0.0389 min^{-1}, which might be owing to the fact that excess Ni-SnS$_2$ could serve as recombination centers, hindering the separation of photogenerated charge.

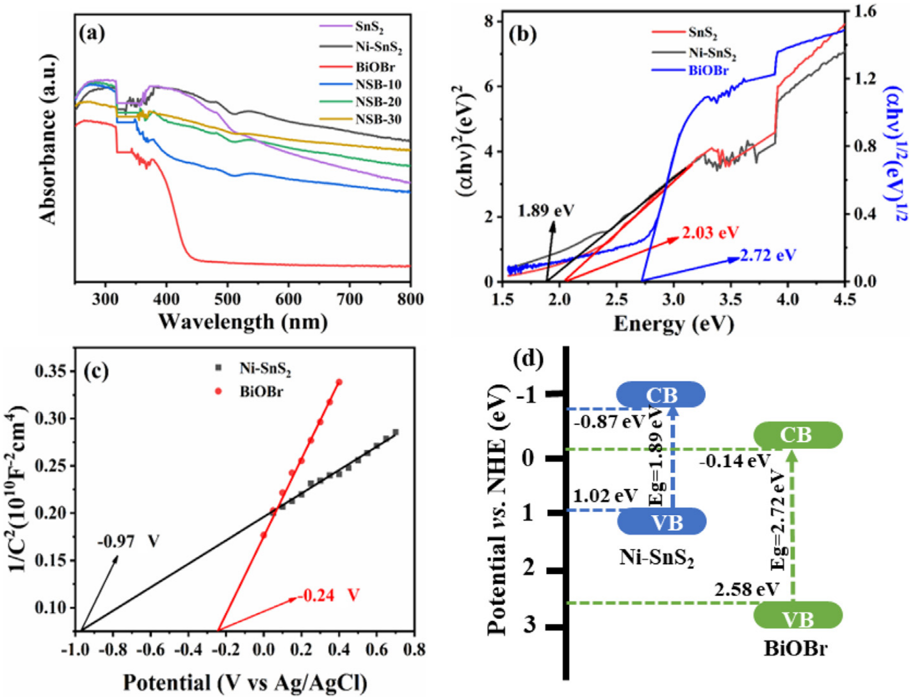

Fig. 5 (a) UV–vis DRS of the as-prepared photocatalysts and (b) Tauc plots of SnS_2, Ni-SnS_2 and BiOBr. (c) Mott-Schottky plots for Ni-SnS_2 and BiOBr, (d) the band structure of single Ni-SnS_2 and BiOBr.

In addition, NSB composites also displayed outstanding photocatalytic activity for RhB degradation. The degradation ratio for RhB on 2D/2D NSB-20 could reach 99.75% after 25 min illumination (Fig. 6c), while the removal rate was only 4.30% and 84.62% when the Ni-SnS_2 and BiOBr sample were employed as the catalyst, respectively. Fig. 6d presents the corresponding rate constants, the order of k from high to low was NSB-20 > SB-20 > NSB-30 > NSB-10 > BiOBr > Ni-SnS_2 > SnS_2. The k value of NSB-20 (0.1894 min^{-1}) was approximately 65.3 and 2.70-folds exceeding of Ni-SnS_2 (0.0029 min^{-1}) and BiOBr (0.0701 min^{-1}), respectively, further demonstrating the synthesized 2D/2D NSB-20 heterojunction possessed much higher photoactivity than single-phase catalyst, which can be used as an efficient photocatalyst for potential wastewater treatment. It is worth noting that the photocatalytic performance of 2D/2D NSB-20 outperforms or is comparable to a wealth of BiOBr-based composite catalysts (Table S1).

The stability and reusability were crucial for an excellent photocatalyst. Thereby, the durability and reusability of sample was appraised with the recycle experiment of NSB-20 nanohybrid. As displayed in Fig. 6e, the NSB-20 nanohybrid still kept high photoactivity (about 90%) with slight decrease after four runs, suggesting the 2D/2D NSB-20 composites was relatively stable in photocatalytic degradation processes. The decreased efficiency may result from the loss of catalyst during the experiment process. In addition, the XRD patterns (Fig. 6f) showed the characteristic peaks do not differ in any significant way after the cycling experiments. These outcomes implied the reusability and stability of the 2D/2D NSB-20 hybrid photocatalysts.

The N_2 adsorption–desorption isotherm and pore size distribution diagrams of all catalysts were shown in Fig. S5. Table S2 depicts the surface area, pore volume, and average pore size. Thereinto, except NSB-10 catalyst, all catalysts had similar average pore sizes, due to the dominant micropore structure of these catalysts. However, the composition and morphology of these catalysts were different, the average pore size cannot represent the photocatalytic performance. Concretely, the Ni-SnS_2 catalyst had a porous flower-like structure, while the BiOBr catalyst showed nanosheets structures with a small number of pore structures. When Ni-SnS_2 was introduced into BiOBr, the flower-like structures composed of a large number of pieces can be obtained. Whereas, compared with other catalysts, the NSB-10 catalyst only formed a small number of mesoporous pores above 4 nm, but no small mesoporous pores of 2 ~ 4 nm. When increasing the amount of Ni-SnS_2, a large number of small mesoporous pores appeared in NSB-20 catalyst, which benefits target molecule adsorption and redox reactions. When continued to add Ni-SnS_2, NSB-30 appeared a certain amount of large mesoporous of 4–30 nm, similar to the pore size distribution of Ni-SnS_2. However, the amount of small mesoporous in NSB-30 decreased, and the catalytic performance was also attenuated. Thus, the catalytic performance was related to the amount of small mesoporous, which was proportional to the specific surface area. As depicted in Fig. S5, the BET specific surface area (S_{BET}) and pore volume of NSB-20 composite was much higher than those of BiOBr and Ni-SnS_2, which was in good agreement with the best photocatalytic activity.

3.3. Effect of different factors on the photodegradation

Generally, the photodegradation of organic pollutants was distinctly influenced by the pH of solution since it could affect the surface charge of catalyst as well as ionization state for con-

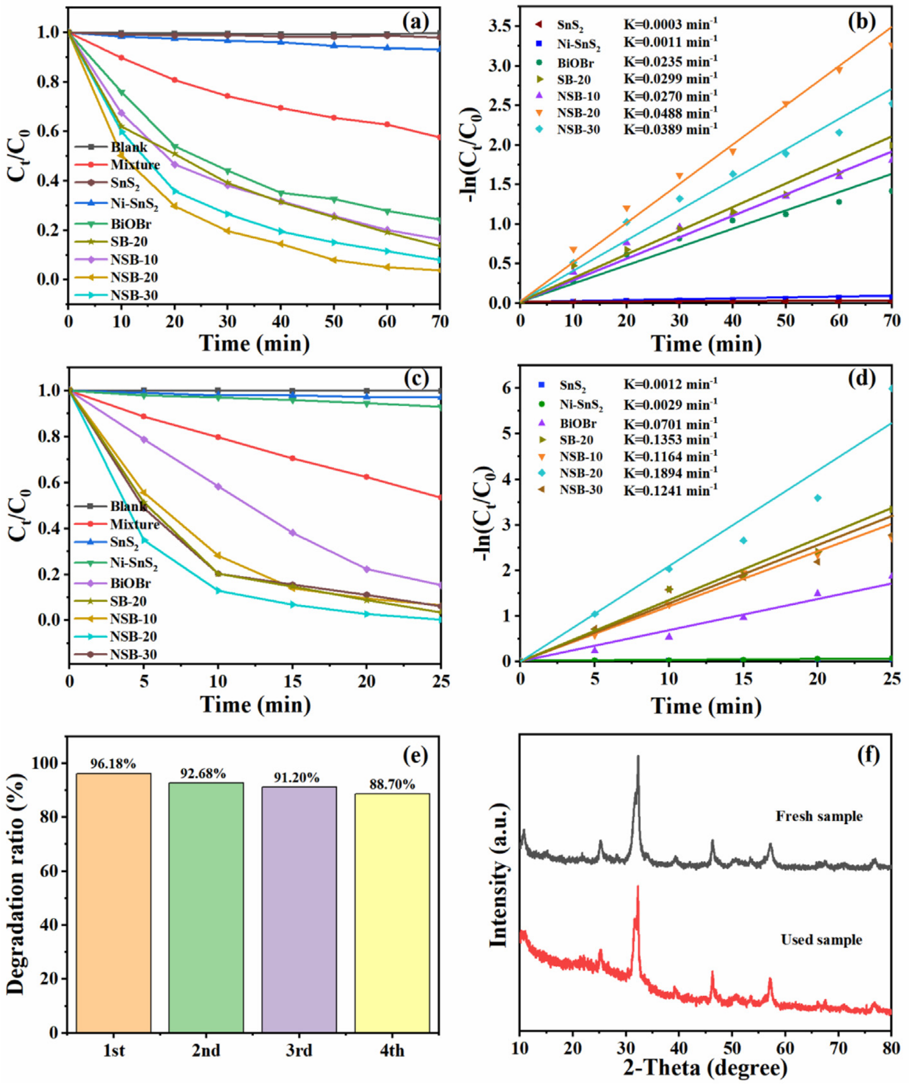

Fig. 6 Photocatalytic degradation curves of TC (a) and RhB (c) over various catalysts, pseudo-first-order kinetic curves for TC (b) and RhB (d) degradation over various catalysts (100 mL 15 mg/L TC or RhB solution, 30 mg photocatalyst, 60 min without sunlight illumination time and 70 or 25 min sunlight illumination time); (e) Recycling tests for the degradation of TC over NSB-20, (f) XRD pattern of fresh and used NSB-20 composite.

taminants. Here, we researched the effect of solution pH on the photodegradation rate of TC by 2D/2D NSB-20. Results showed that the highest decomposition rate achieved at pH = 5, while it gradually declined as the pH rose (Fig. 7a). The zeta potential measurement for 2D/2D NSB-20 hybrid was depictured in Fig. 7b. The point of zero charge (pH$_{pzc}$) of NSB-20 was about 7.9. Hence, 2D/2D NSB-20 nanohybrid was positively charged at pH < 7.9, while negatively charged at pH > 7.9. TC molecule could form three kinds of species in aqueous solution with various pH (Dou, X. et al., 2022; Yu, H. et al., 2020), such as cationic substance TCH_3^+ (pH < 3.3), neutral substance TCH_2^0 (3.3 < pH < 7.7), as well as anionic substance TCH_3^- (pH > 7.7). When the reaction solution pH was > 7.9, TC molecule and NSB-20 hybrids repelled each other because both of them were negatively charged. This could explain why at higher pH the lower degradation efficiency of TC. Here, the solution pH value was adjusted with NaOH solution to 7, the competitive adsorption onto the catalyst between ions from NaOH and pollutants resulted in the decreased removal rate (Jia, X. et al., 2020). Thereby, the order of decomposition rate of TC relying on solution pH was determined to be pH 5 (natural pH) > pH 7 > pH 9 > pH 11.

The effect of different foreign anions (Cl^-, SO_4^{2-}, CO_3^{2-} and NO_3^-) on TC degradation by NSB-20 was investigated. Fig. 7c displays that the presence of Cl^- and NO_3^- exhibited negligible effect on the TC removal. The existence of SO_4^{2-} has a slightly negative effect on the TC degradation because SO_4^{2-} might compete with TC molecules for adsorption. Nevertheless, the decomposition rate of TC was only 16.91% after addition of CO_3^{2-}. This phenomenon can be ascribed to the strong quenching effect of CO_3^{2-} on hydroxyl radical (Xiao, H. et al., 2008). The influences of initial TC concentration on the photoactivity were also analyzed. Fig. 7d exhibits the degradation of TC with different concentrations over NSB-20. The TC removal rate dropped from 99.35% to 67.43% when initial TC concentration increased from 10 to 25 mg/L.

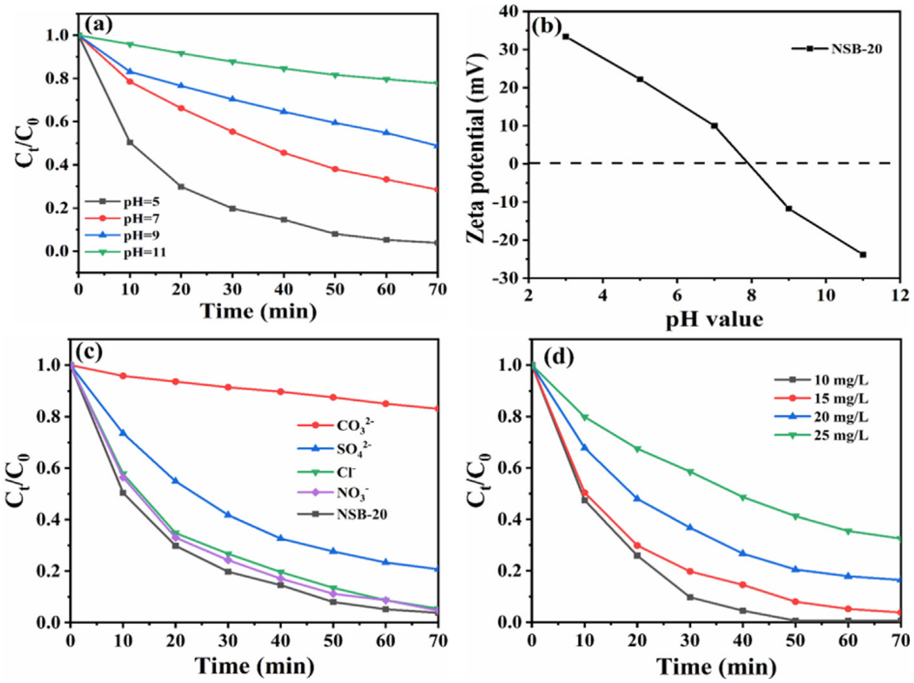

Fig. 7 (a) Effect of solution pH on the degradation of TC over NSB-20, (b) Zeta potentials of NSB-20, Effects of inorganic salts ions (c) and initial concentration (d) on the removal of TC over NSB-20.

The high concentration of TC quickly exhausts the reactive species produced by NSB-20, so the degradation rate would reduce when NSB-20 cannot generate enough active species (Liu, J. et al., 2021).

3.4. Photocatalysis mechanism

To better comprehend the enhancement in photocatalytic activity of 2D/2D NSB composite, photoluminescence (PL) spectra was used to research the photocarriers segregation efficiency of catalysts. Generally, the lower PL intensity represents the stronger segregation efficiency of carriers (Cui, H. et al., 2021). Fig. 8a depicts that the PL peak for BiOBr was centered at approximately 440 nm, which may result from the band-band PL phenomenon with light energy approximately equivalent to the E_g of BiOBr. The PL intensity of NSB catalysts was much weaker than that of BiOBr, indicating that the construction of heterojunctions can effectively inhibit the recombination of photocarriers. This effect was most pronounced for NSB-20 hybrid, which agreed well with the highest photocatalytic performance. Transient photocurrents response (TPR) and electrochemical impedance spectra (EIS) were employed to analyze the segregation and migration ability of carriers in the catalyst. The TPR was documented through repeatedly switching on and off at open-circuit potential under light illumination. In general, the higher TPR represents the higher photocarrier segregation efficiency (Su, Y. et al., 2022). Fig. 8b displays that the 2D/2D NSB-20 nanohybrid exhibited the highest photocurrent intensity, suggesting it had highly improved photocarrier segregation capability. Meanwhile, the EIS analysis uncovered that the 2D/2D NSB-20 owned the smallest radius of curvature (Fig. 8c), suggesting its interfacial transfer resistance was the smallest and interfacial charge transfer rate was highest (Liu, L. et al., 2021).

In general, active/radical substances like holes (h^+), hydroxyl radical (•OH), and superoxide anion radicals (•O_2^-) play a vital role in pollutant degradation. In order to reveal reaction mechanism of TC removal, Isopropanol (IPA) (Sreeram, N. et al., 2022), triethanolamine (TEOA) (Zhang, X. et al., 2022) and benzoquinone (BQ) (Sun, H. et al., 2020) were selected as the scavenging agents for •OH, h^+ as well as •O_2^-, respectively. Fig. 9a and b depicts that the degradation rate of TC declined to 16.37% and 33.46%, respectively, after BQ and TEOA added in the reaction solution, reflecting h^+ and •O_2^- were vital active species in TC degradation by NSB-20. Nevertheless, the introduction of IPA lead to a slight decrease in degradation efficiency (Fig. 9a and b). This indicated that •OH also worked in the photodegradation of TC. The radicals produced in the photocatalytic system were further studied by ESR, and the 5, 5-dimethyl-1-pyrroline-N-oxide (DMPO) reagent was applied to trap •OH and •O_2^-. As shown in Fig. 9c-d, no signal peak was observed under dark conditions, however, with VL irradiation for 10 min, four characteristic peaks of DOMP- •O_2^- and four peaks of DMPO-•OH with the intensity of 1:2:2:1 were detected (Fig. 9d). Hence, the result of EPR tests verified the formation of •O_2^- and •OH in the system, well agreeing with the outcomes of radical capture measurements.

To explore the decomposition routes of TC, the intermediate products produced during the photocatalytic reaction were identified by liquid chromatography-mass spectrometry (LC-MS). Thirteen major intermediate products (P1-P13) were proposed by photocatalytic removal of TC, and their *m*/*z* values were 476 (P1), 417 (P2), 370 (P3), 222 (P4), 458 (P5), 398 (P6), 359 (P7), 337 (P8), 226 (P9), 368 (P10), 361 (P11), 316 (P12) and 213 (P13) (Fig. S6). According to the products observed from the mass spectra, three possible decomposition routes of TC over NSB-20 were inferred (Fig. 10) (Zhang, W.

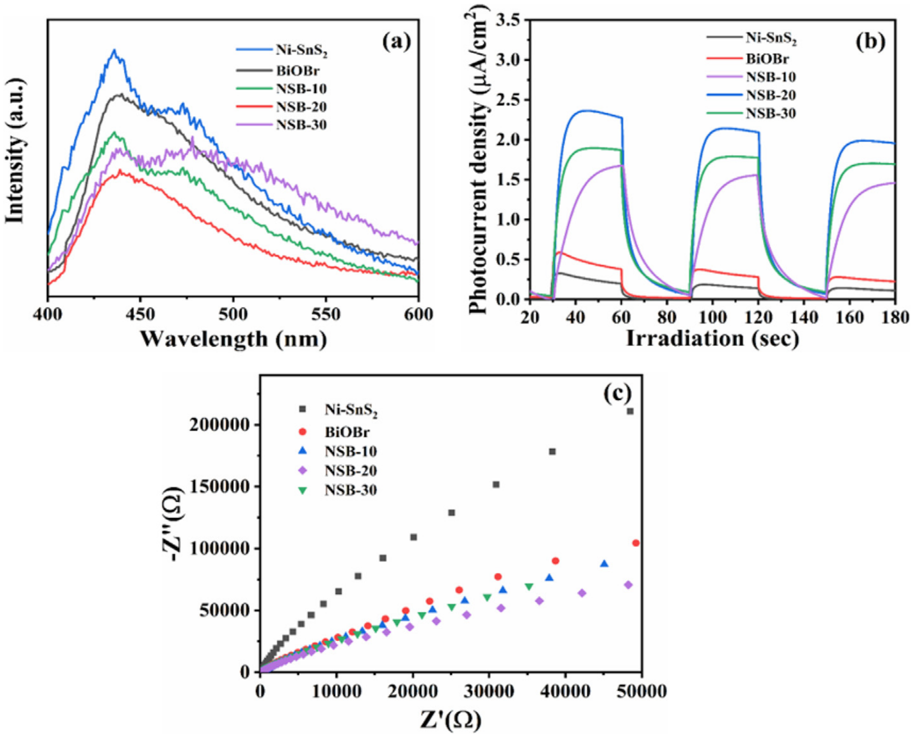

Fig. 8 (a) PL spectra (λ_{ex} = 375 nm), (b) transient photocurrent responses and (c) EIS spectra of Ni-SnS$_2$, BiOBr and NSB composites.

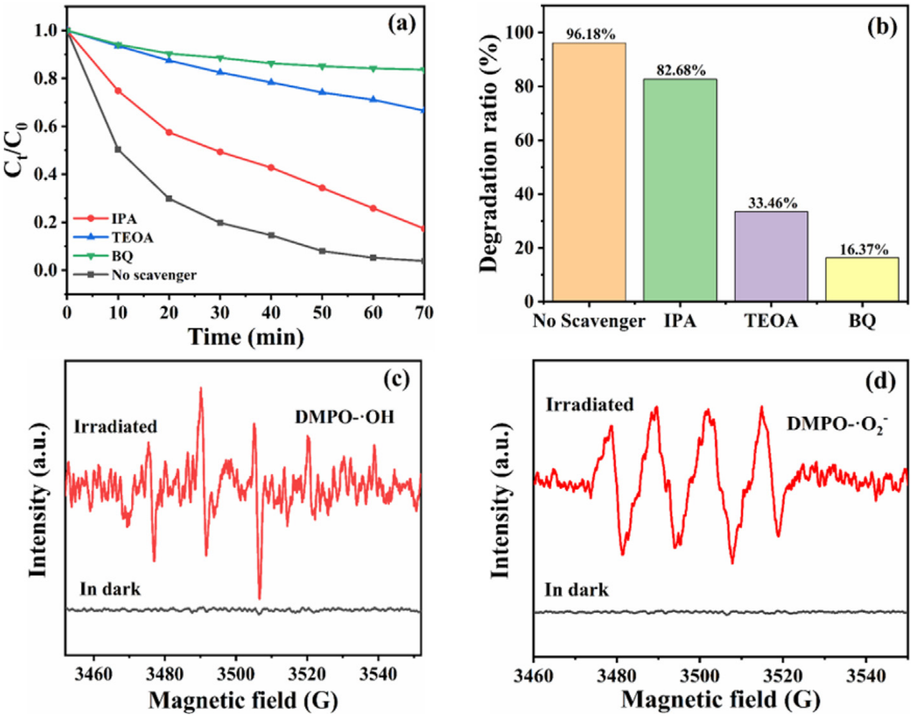

Fig. 9 (a) Degradation curves, (b) degradation ratios of TC by NSB-20 in the presence of various scavengers and ESR spectra of (c) DMPO-•OH and (d) DMPO-•O_2^-.

et al., 2022). For the pathway I, the C = C double bonds in TC were hydroxylated through an addition reaction in the presence of •OH to afford P5. Then, demethylation of the dimethylamino group proceeded under the attack of •O_2^- and h^+ to give P6. Hereafter, a series of reactions (i.e., deamination, loss of amide group, ring-cleavage reaction) occurred progressively, leading to the formation of P7, P8 and P9, respectively. In terms of pathway II, TC was converted into

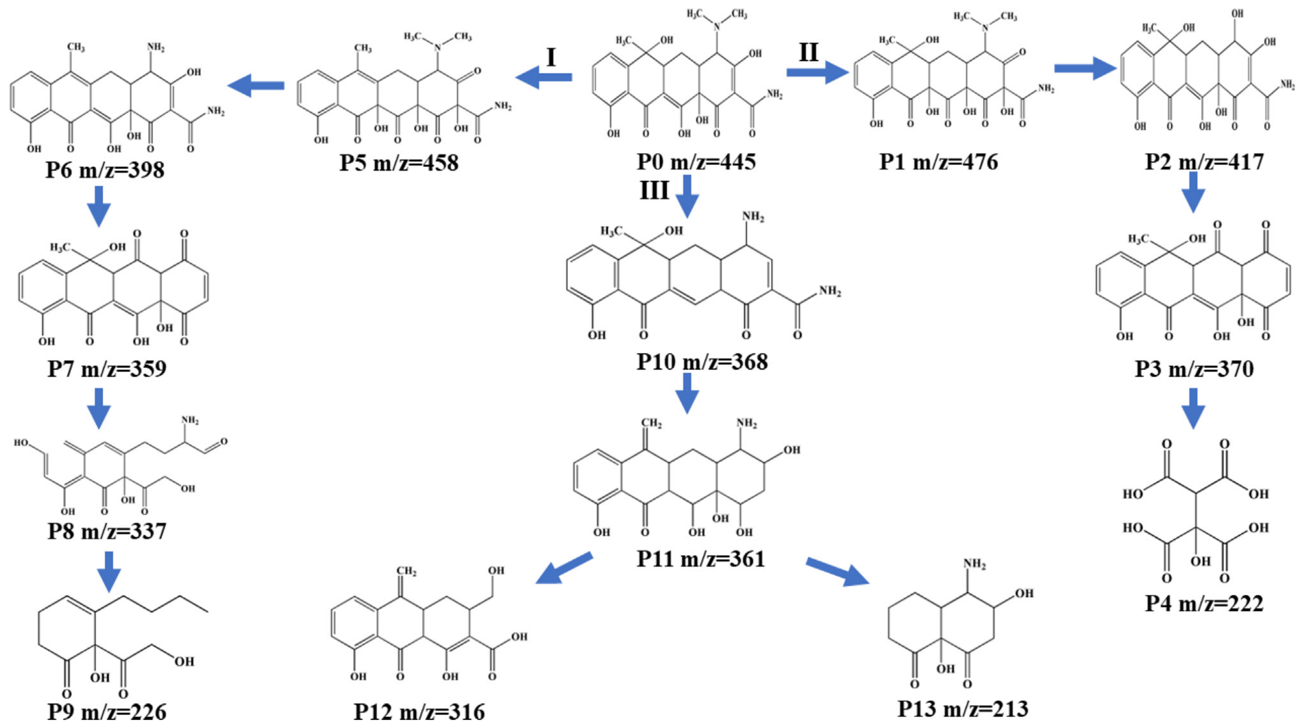

Fig. 10 Possible degradation pathways of TC on NSB-20.

P1 through similar hydroxylation reactions as observed in pathway I. The resulting P1 was decomposed into P2 by losing the saturated -N(CH_3)$_2$ moiety under the attacked of $\bullet O_2^-$. Subsequently, the degradation of P2 to P3 was achieved via cleavage of the amide and hydroxyl groups. In the presence of •OH, unstable P3 underwent ring-cleavage reactions to generate small molecule P4. In pathway III, TC was first transformed into P10 by demethylation of the dimethylamino group to release amino group. Cleavage of the hydroxyl group on the cyclohexanone moiety and loss of the amide group then proceeded under attack by $\bullet O_2^-$ and h^+ to generate P11, which was further degraded into P12 and P13 via the ring-opening and deamination reaction. Finally, these intermediates were eventually degraded into small molecules, as verified by the TOC outcomes.

In light of the aforementioned results and analysis, a probable mechanism was put forward to illuminate the remarkable photocatalytic property of 2D/2D NSB-20 heterojunction. As illustrated in Fig. S7, when irradiated by VL, the e^- of BiOBr and Ni-SnS_2 were excited to their respective CB while leaving h^+ on the VB. Assuming the type-II heterojunction was constructed between constituents, the e^- in the CB of Ni-SnS_2 would move to BiOBr, and the h^+ would migrate from the VB of BiOBr to Ni-SnS_2. Nevertheless, the accumulated e^- in the CB of BiOBr cannot reduce O_2 to produce $\bullet O_2^-$ ($O_2/\bullet O_2^-$ = −0.33 eV vs. NHE) due to its unsuitable CB potential. Meanwhile, the h^+ in the VB of Ni-SnS_2 could not provide enough driving force for generation of •OH radicals since the E_{VB} of Ni-SnS_2 (1.02 eV vs. NHE) was more negative than the potential of $H_2O/\bullet OH$ (2.27 eV vs. NHE) (Xing, Y. et al., 2022). These were inconsistent with the outcomes of active species capture tests, where •OH and $\bullet O_2^-$ were significant species in TC decomposition. Thereupon, the traditional type-II heterojunction was ruled out for this system, and the S-scheme mechanism may be more rational to elaborate photoinduced charges migration and excellent photocatalytic activity.

The density functional theory (DFT) calculations were used to analyze the interfacial charge transfer between BiOBr and Ni-SnS_2. As displayed in Fig. 11a-b, the work functions of BiOBr (0 0 1) crystal planes and Ni-SnS_2 (0 0 1) surface were calculated as 6.4 eV and 5.7 eV, respectively, suggesting that the photoinduced electrons in Ni-SnS_2 nanosheets could flow to the BiOBr nanosheets through the 2D/2D heterojunction. From Fig. 11c, planar-averaged charge density displayed that the electrons migrate from Ni-SnS_2 (0 0 1) to BiOBr (0 0 1) surface when Ni-SnS_2/BiOBr heterojunction formed, which is further verified by the charge density difference (Fig. 11d). The above outcomes suggested that BiOBr exhibited much higher work functions than that of Ni-SnS_2, therefore the two catalysts were available to form S-scheme heterojunctions with an improved charge migration behavior. Fig. 12 presents the S-scheme heterojunction of Ni-SnS_2/BiOBr along with the charge transfer and separation process. Before contact, Ni-SnS_2 exhibits a more-negative E_f compared with BiOBr since its work function is smaller than BiOBr. After Ni-SnS_2 and BiOBr are coupled to construct heterojunctions, the electrons from Ni-SnS_2 spontaneously migrate to BiOBr until their E_f reached an equal level. This electron transfer path results in the generation of an internal electric field (IEF), which directed from Ni-SnS_2 to BiOBr. At the heterojunction interfaces, the surface of Ni-SnS_2 and BiOBr is positively charged and negatively charged, respectively. When Ni-SnS_2/BiOBr heterojunctions are illuminated by VL, both Ni-SnS_2 and BiOBr are photoinduced to produce e^- and h^+ (Eq. (1)). The useless e^- in the CB of BiOBr tend to recombine with relatively useless h^+ in the VB of Ni-SnS_2 via the intimate interface under the driving force of the IEF (Eq. (2)), while preserving useful e^- and h^+ with high redox ability in the VB of BiOBr and CB

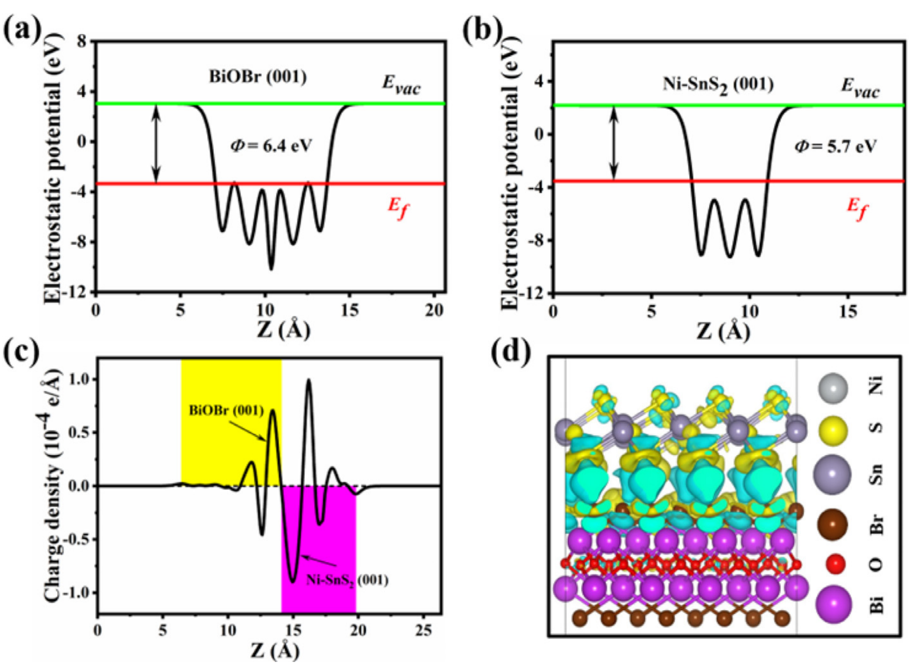

Fig. 11 Electrostatic potentials of (a) BiOBr (0 0 1) surface and (b) Ni-doped SnS_2 (0 0 1) surface. (c) Planar-averaged charge density for Ni-SnS_2/BiOBr. The yellow and purple areas indicate electron accumulation and depletion, respectively; (d) The charge density difference for Ni-SnS_2/BiOBr.

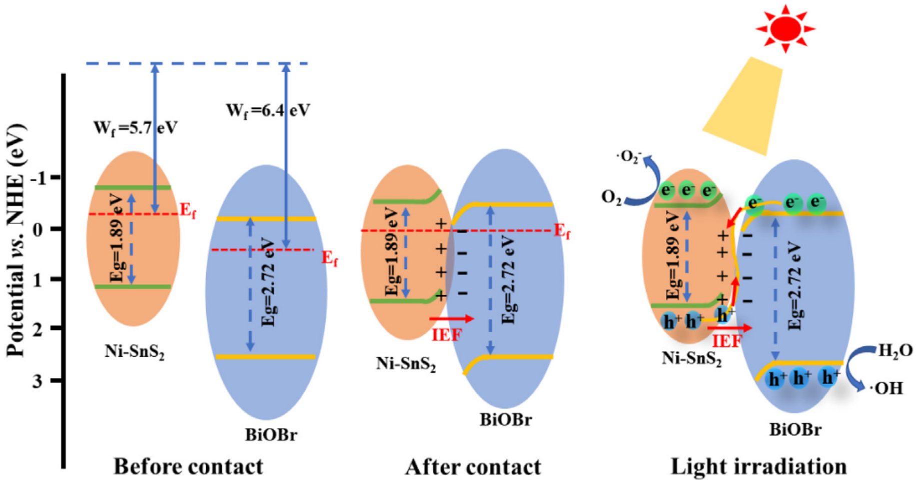

Fig. 12 Band energy positions of Ni-SnS_2 and BiOBr before contact, after contact and S-scheme charge transfer mechanism between Ni-SnS_2 and BiOBr under irradiation.

of Ni-SnS_2, respectively. This process contributes to highly improved photocarrier separation efficiency. The e$^-$ in the CB of Ni-SnS_2 can react with O_2 to form •O_2^- (Eq. (3)), and the h$^+$ in the VB of BiOBr can react with H_2O or OH^- to form •OH (Eq. (4)). Thereafter, these active substances would engage in TC or RhB degradation (Eq. (5)). In addition, the 2D/2D heterostructures also make contributions to the outstanding photoactivity of NSB-20. This 2D/2D interface supply stronger interaction between Ni-SnS_2 and BiOBr with a tight and large contact interface, which is conductive to the photocarrier separation and migration.

$$\mathrm{NSB} + hv \rightarrow \mathrm{NSB}\ (e^-, h^+) \quad (1)$$

$$h^+(\text{Ni-SnS}_2) + e^-(\mathrm{BiOBr}) \rightarrow \text{Reunion} \quad (2)$$

$$h^+\ (\mathrm{BiOBr}) + H_2O \text{ or } OH^- \rightarrow \bullet OH \quad (3)$$

$$e^-(\text{Ni-SnS}_2) + O_2 \rightarrow \bullet O_2^- \quad (4)$$

$$\text{TC or RhB} + \bullet OH/\bullet O_2^- \rightarrow \text{Degradation products} \quad (5)$$

4. Conclusions

In conclusion, a novel 2D/2D NSB S-scheme composite photocatalyst was successfully synthesized by a simple in-situ precipitation approach. The NSB nanohybrids exhibited remarkably boosted photocatalytic properties compared to single-phase catalysts. Among all the catalysts, the NSB-20 displayed the highest photoactivity for the removal of TC and RhB. The rate constant of TC over the 2D/2D NSB-20 heterojunction was 0.0488 min^{-1}, which reached up to 44.36 and 2. 07 time as much as than those of 2D Ni-SnS_2 and 2D BiOBr, respectively. The splendid property originated from the tight 2D/2D interface contact, excellent optical response, abundant active sites and the construction of S-scheme heterojunction, which not only promoted spatial segregation of photocarriers but also preserved strong redox power. In addition, the 2D/2D NSB-20 nanohybrid showed high stability and reusability. The S-scheme charge transfer mechanism was put forward to explain the boosted photocatalytic activity based on the trapping tests, ESR experiments along with DFT calculation. This investigation offers a new insight to designing efficient 2D/2D S-scheme photocatalyst for water purification.

Declaration of Competing Interest

The authors declare that they have no known competing financial interests or personal relationships that could have appeared to influence the work reported in this paper.

Acknowledgments

This work was supported by the Foundation of Educational Commission of Anhui Province, PR China (KJ2021A0518, 2022AH050376), the Quality Engineering (2021zlgc015) and National innovation and Entrepreneurship training program for college students, PR China (202110373034).

Appendix A. Supplementary material

Supplementary data to this article can be found online at https://doi.org/10.1016/j.arabjc.2023.105081.

References

Arunkumar, M., Veerakumar, S., Mohanavel, V., Vairamuthu, J., Vijayan, V., Senthilkumar, N., 2021. A novel visible light-driven p-type $BiFeO_3$/n-type SnS_2 heterojunction photocatalyst for efficient charge separation and enhanced photocatalytic activity. J. Clust. Sci. 32, 1431–1439. https://doi.org/10.1007/s10876-021-02114-4.

Chang, C.-J., Huang, C.-L., Yu, Y.-H., Teng, M.-C., Chiang, C.-L., Lin, Y.-G., 2022. Electron transfer dynamics and enhanced H_2 production activity of hydrangea-like BiOBr/Bi_2S_3-based photocatalysts with Cu-complex as a redox mediator. Appl. Surf. Sci. 576,. https://doi.org/10.1016/j.apsusc.2021.151870 151870.

Chen, D., Huang, S., Huang, R., Zhang, Q., Le, T.T., Cheng, E., Yue, R., Hu, Z., Chen, Z., 2019. Construction of Ni-doped SnO_2-SnS_2 heterojunctions with synergistic effect for enhanced photodegradation activity. J. Hazard. Mater. 368, 204–213. https://doi.org/10.1016/j.jhazmat.2019.01.009.

Chen, N., Jia, X., He, H., Lin, H., Guo, M., Cao, J., Zhang, J., Chen, S., 2022. Promoting photocarriers separation in S-scheme system with Ni_2P electron bridge: The case study of BiOBr/Ni_2P/g-C_3N_4. Chin. J. Catal. 43, 276–287. https://doi.org/10.1016/s1872-2067(21)63817-2.

Chen, C., Zang, J., Wang, Q., Li, Y., 2021. Loading SnS_2 nanosheets decorated with MoS_2 nanoparticles on a flake-shaped g-C_3N_4 network for enhanced photocatalytic performance. CrystEngComm 23, 4680–4693. https://doi.org/10.1039/d1ce00385b.

Cotillas, S., Llanos, J., Cañizares, P., Clematis, D., Cerisola, G., Rodrigo, M.A., Panizza, M., 2018. Removal of Procion Red MX-5B dye from wastewater by conductive-diamond electrochemical oxidation. Electrochim. Acta 263, 1–7. https://doi.org/10.1016/j.electacta.2018.01.052.

Cui, H., Dong, S., Wang, K., Luan, M., Huang, T., 2021. Synthesis of a novel Type-II In_2S_3/Bi_2MoO_6 heterojunction photocatalyst: Excellent photocatalytic performance and degradation mechanism for Rhodamine B. Sep. Purif. Technol. 255,. https://doi.org/10.1016/j.seppur.2020.117758 117758.

Dou, X., Zhang, C., Shi, H., 2022. The simultaneous promotion of Cr (VI) photoreduction and tetracycline removal over 3D/2D Cu_2O/BiOBr S-scheme nanostructures. Sep. Purif. Technol. 282,. https://doi.org/10.1016/j.seppur.2021.120023 120023.

Dou, X., Chen, Y., Shi, H., 2022. $CuBi_2O_4$/BiOBr composites promoted PMS activation for the degradation of tetracycline: S-scheme mechanism boosted Cu^{2+}/Cu^{+} cycle. Chem. Eng. J. 431,. https://doi.org/10.1016/j.cej.2021.134054 134054.

Du, C., Nie, S., Zhang, C., Wang, T., Wang, S., Zhang, J., Yu, C., Lu, Z., Dong, S., Feng, J., Liu, H., Sun, J., 2022. Dual-functional Z-scheme CdSe/Se/BiOBr photocatalyst: Generation of hydrogen peroxide and efficient degradation of ciprofloxacin. J. Colloid Interf. Sci. 606, 1715–1728. https://doi.org/10.1016/j.jcis.2021.08.152.

Hasanvandian, F., Moradi, M., Aghaebrahimi Samani, S., Kakavandi, B., Rahman Setayesh, S., Noorisepehr, M., 2022. Effective promotion of g-C_3N_4 photocatalytic performance via surface oxygen vacancy and coupling with bismuth-based semiconductors towards antibiotics degradation. Chemosphere 287,. https://doi.org/10.1016/j.chemosphere.2021.132273 132273.

Hasanvandian, F., Shokri, A., Moradi, M., Kakavandi, B., Rahman Setayesh, S., 2022. Encapsulation of spinel $CuCo_2O_4$ hollow sphere in V_2O_5-decorated graphitic carbon nitride as high-efficiency double Z-type nanocomposite for levofloxacin photodegradation. J. Hazard. Mater. 423,. https://doi.org/10.1016/j.jhazmat.2021.127090 127090.

Hayati, F., Moradi, S., Farshineh Saei, S., Madani, Z., Giannakis, S., Isari, A.A., Kakavandi, B., 2022. A novel, Z-scheme ZnO@AC@-FeO photocatalyst, suitable for the intensification of photo-mediated peroxymonosulfate activation: Performance, reactivity and bisphenol A degradation pathways. J. Environ. Manage. 321,. https://doi.org/10.1016/j.jenvman.2022.115851 115851.

He, C., Shi, Y., Feng, B., Ruan, S., Qin, C., Xu, K., Zhang, L., 2023. Catalytic combustion kinetics of methyl butanoate over Pd/γ-Al_2O_3 catalysts: An experimental and theoretical study. Chem. Eng. Sci. 269,. https://doi.org/10.1016/j.ces.2023.118489 118489.

He, S., Zhai, C., Fujitsuka, M., Kim, S., Zhu, M., Yin, R., Zeng, L., Majima, T., 2021. Femtosecond time-resolved diffuse reflectance study on facet engineered charge-carrier dynamics in Ag_3PO_4 for antibiotics photodegradation. Appl. Catal. B: Environ. 281,. https://doi.org/10.1016/j.apcatb.2020.119479 119479.

Jia, X., Han, Q., Liu, H., Li, S., Bi, H., 2020. A dual strategy to construct flowerlike S-scheme BiOBr/$BiOAc_{1-x}Br_x$ heterojunction with enhanced visible-light photocatalytic activity. Chem. Eng. J. 399,. https://doi.org/10.1016/j.cej.2020.125701 125701.

Kumar, G., Dutta, R.K., 2022. Fabrication of plate-on-plate SnS_2/Bi_2WO_6 nanocomposite as photocatalyst for sunlight mediated degradation of antibiotics in aqueous medium. J Phys Chem Solids 164,. https://doi.org/10.1016/j.jpcs.2022.110639 110639.

Li, S., Cai, M., Liu, Y., Wang, C., Yan, R., Chen, X., 2023. Constructing $Cd_{0.5}Zn_{0.5}S$/Bi_2WO_6 S-scheme heterojunction for boosted photocatalytic antibiotic oxidation and Cr(VI) reduction. Adv. Powder Mater. 2,. https://doi.org/10.1016/j.apmate.2022.100073 100073.

Li, M., Li, D., Zhou, Z., Wang, P., Mi, X., Xia, Y., Wang, H., Zhan, S., Li, Y., Li, L., 2020. Plasmonic Ag as electron-transfer mediators in Bi_2MoO_6/Ag-AgCl for efficient photocatalytic inactivation of bacteria. Chem. Eng. J. 382,. https://doi.org/10.1016/j.cej.2019.122762 122762.

Li, Y., Liu, Y., Xing, D., Wang, J., Zheng, L., Wang, Z., Wang, P., Zheng, Z., Cheng, H., Dai, Y., Huang, B., 2021. 2D/2D heterostructure of ultrathin $BiVO_4$/Ti_3C_2 nanosheets for photocatalytic overall Water splitting. Appl. Catal. B: Environ. 285,. https://doi.org/10.1016/j.apcatb.2020.119855 119855.

Li, S., Wang, C., Liu, Y., Cai, M., Wang, Y., Zhang, H., Guo, Y., Zhao, W., Wang, Z., Chen, X., 2022. Photocatalytic degradation of tetracycline antibiotic by a novel $Bi_2Sn_2O_7$/Bi_2MoO_6 S-scheme heterojunction: Performance, mechanism insight and toxicity assessment. Chem. Eng. J. 429,. https://doi.org/10.1016/j.cej.2021.132519 132519.

Li, S., Wang, C., Cai, M., Yang, F., Liu, Y., Chen, J., Zhang, P., Li, X., Chen, X., 2022. Facile fabrication of TaON/Bi_2MoO_6 core–shell S-scheme heterojunction nanofibers for boosting visible-light catalytic levofloxacin degradation and Cr(VI) reduction. Chem. Eng. J. 428,. https://doi.org/10.1016/j.cej.2021.131158 131158.

Li, W., Xu, Q., Chen, W., Gou, F., Zhou, S., Li, J., Qi, C., Ma, D.K., 2021. Vertical growth of SnS_2 nanobelt arrays on $CuSbS_2$ nanosheets for enhanced photocatalytic reduction of CO_2. Chem Commun (Camb) 57, 10419–10422. https://doi.org/10.1039/d1cc04584a.

Li, Q., Xue, D.X., Zhang, Y.F., Zhang, Z.H., Wang, Q., Gao, Z.W., Bai, J.F., 2017. A copper-organic framework as scavenger towards organic dyes pollutants via physical adsorption and visible-light photodegradation. Inorg. Chem. Commun. 85, 78–83. https://doi.org/10.1016/j.inoche.2017.06.021.

Liang, L., Gao, S., Zhu, J., Wang, L., Xiong, Y., Xia, X., Yang, L., 2020. The enhanced photocatalytic performance toward carbamazepine by nitrogen-doped carbon dots decorated on BiOBr/CeO_2: Mechanism insight and degradation pathways. Chem. Eng. J. 391,. https://doi.org/10.1016/j.cej.2019.123599 123599.

Ling, Y.L., Dai, Y.Z., 2020. Direct Z-scheme hierarchical WO_3/BiOBr with enhanced photocatalytic degradation performance under visible light. Appl. Surf. Sci. 509,. https://doi.org/10.1016/j.apsusc.2019.145201 145201.

Liu, E., Chen, J., Ma, Y., Feng, J., Jia, J., Fan, J., Hu, X., 2018. Fabrication of 2D SnS_2/g-C_3N_4 heterojunction with enhanced H_2 evolution during photocatalytic water splitting. J Colloid Interface Sci 524, 313–324. https://doi.org/10.1016/j.jcis.2018.04.038.

Liu, L., Dai, K., Zhang, J., Li, L., 2021. Plasmonic Bi-enhanced ammoniated alpha-MnS/Bi_2MoO_6 S-scheme heterostructure for visible-light-driven CO_2 reduction. J. Colloid Interf. Sci. 604, 844–855. https://doi.org/10.1016/j.jcis.2021.07.064.

Liu, H., Du, C., Bai, H., Su, Y., Wei, D., Wang, Y., Liu, G., Yang, L., 2018. Fabrication of plate-on-plate Z-scheme SnS_2/Bi_2MoO_6 heterojunction photocatalysts with enhanced photocatalytic activity. J. Mater. Sci. 53, 10743–10757. https://doi.org/10.1007/s10853-018-2296-2.

Liu, Y., He, J., Qi, Y., Wang, Y., Long, F., Wang, M., 2022. Preparation of flower-like BiOBr/Bi_2WO_6 Z-scheme heterojunction through an ion exchange process with enhanced photocatalytic activity. Mat. Sci. Semicon. Proc. 137,. https://doi.org/10.1016/j.mssp.2021.106195 106195.

Liu, J., Huang, L., Li, Y., Yang, L., Wang, C., Liu, J., Song, Y., Yang, M., Li, H., 2021. Construction of oxygen vacancy assisted Z-scheme BiO_{2-x}/BiOBr heterojunction for LED light pollutants degradation and bacteria inactivation. J. Colloid Interf. Sci. 600, 344–357. https://doi.org/10.1016/j.jcis.2021.04.143.

Liu, P., Wu, Z., Abramova, A.V., Cravotto, G., 2021. Sonochemical processes for the degradation of antibiotics in aqueous solutions: A review. Ultrason Sonochem 74,. https://doi.org/10.1016/j.ultsonch.2021.105566 105566.

Lv, X., Yan, D.Y.S., Lam, F.-L.-Y., Ng, Y.H., Yin, S., An, A.K., 2020. Solvothermal synthesis of copper-doped BiOBr microflowers with enhanced adsorption and visible-light driven photocatalytic degradation of norfloxacin. Chem. Eng. J. 401,. https://doi.org/10.1016/j.cej.2020.126012 126012.

Meng, J., Duan, Y., Jing, S., Ma, J., Wang, K., Zhou, K., Ban, C., Wang, Y., Hu, B., Yu, D., Gan, L., Zhou, X., 2022. Facet junction of BiOBr nanosheets boosting spatial charge separation for CO_2 photoreduction. Nano Energy 92,. https://doi.org/10.1016/j.nanoen.2021.106671 106671.

Miao, Z., Wang, Q., Zhang, Y., Meng, L., Wang, X., 2022. In situ construction of S-scheme AgBr/BiOBr heterojunction with surface oxygen vacancy for boosting photocatalytic CO_2 reduction with H_2O. Appl. Catal. B: Environ. 301,. https://doi.org/10.1016/j.apcatb.2021.120802 120802.

Murugalakshmi, M., Saravanakumar, K., Park, C.M., Muthuraj, V., 2022. Efficient photocatalytic degradation of sulfasalazine and reduction of hexavalent chromium over robust In_2S_3/Nd_2O_3 heterojunction under visible light. J. Water Process Eng. 45,. https://doi.org/10.1016/j.jwpe.2021.102492 102492.

Ni, J., Liu, D., Wang, W., Wang, A., Jia, J., Tian, J., Xing, Z., 2021. Hierarchical defect-rich flower-like BiOBr/Ag nanoparticles/ultrathin g-C_3N_4 with transfer channels plasmonic Z-scheme heterojunction photocatalyst for accelerated visible-light-driven photothermal-photocatalytic oxytetracycline degradation. Chem. Eng. J. 419,. https://doi.org/10.1016/j.cej.2021.129969 129969.

Qiu, F., Li, W., Wang, F., Li, H., Liu, X., Sun, J., 2017. In-situ synthesis of novel Z-scheme SnS_2/BiOBr photocatalysts with superior photocatalytic efficiency under visible light. J. Colloid Interf. Sci. 493, 1–9. https://doi.org/10.1016/j.jcis.2016.12.066.

Senasu, T., Nijpanich, S., Juabrum, S., Chanlek, N., Nanan, S., 2021. CdS/BiOBr heterojunction photocatalyst with high performance for solar-light-driven degradation of ciprofloxacin and norfloxacin antibiotics. Appl. Surf. Sci. 567,. https://doi.org/10.1016/j.apsusc.2021.150850 150850.

Shanmugaratnam, S., Selvaratnam, B., Baride, A., Koodali, R., Ravirajan, P., Velauthapillai, D., Shivatharsiny, Y., 2021. SnS_2/TiO_2 nanocomposites for hydrogen production and photodegradation under extended solar irradiation. Catalysts 11, 589. https://doi.org/10.3390/catal11050589.

Shao, B., Liu, Z., Zeng, G., Liu, Y., Liang, Q., He, Q., Wu, T., Pan, Y., Huang, J., Peng, Z., Luo, S., Liang, C., Liu, X., Tong, S., Liang, J., 2021. Synthesis of 2D/2D CoAl-LDHs/$Ti_3C_2T_x$ Schottky-junction with enhanced interfacial charge transfer and visible-light photocatalytic performance. Appl. Catal. B: Environ. 286,. https://doi.org/10.1016/j.apcatb.2020.119867 119867.

Shao, B., Liu, Z., Tang, L., Liang, Q., He, Q., Wu, T., Pan, Y., Cheng, M., Liu, Y., Tan, X., Tang, J., Wang, H., Feng, H., Tong, S., 2022. Construction of Bi_2WO_6/CoAl-LDHs S-scheme heterojunction with efficient photo-Fenton-like catalytic performance: Experimental and theoretical studies. Chemosphere 291,. https://doi.org/10.1016/j.chemosphere.2021.133001 133001.

Sin, J.-C., Lam, S.-M., Zeng, H., Lin, H., Li, H., Tham, K.-O., Mohamed, A.R., Lim, J.-W., Qin, Z., 2021. Magnetic $NiFe_2O_4$ nanoparticles decorated on N-doped BiOBr nanosheets for expeditious visible light photocatalytic phenol degradation and hexavalent chromium reduction via a Z-scheme heterojunction mechanism. Appl. Surf. Sci. 559,. https://doi.org/10.1016/j.apsusc.2021.149966 149966.

Song, S., Wu, K., Wu, H., Guo, J., Zhang, L., 2020. Synthesis of Z-scheme multi-shelled ZnO/$AgVO_3$ spheres as photocatalysts for the degradation of ciprofloxacin and reduction of chromium(VI). J. Mater. Sci. 55, 4987–5007. https://doi.org/10.1007/s10853-019-04316-8.

Sreeram, N., Aruna, V., Koutavarapu, R., Lee, D.Y., Shim, J., 2022. Visible-light-driven indium vanadium oxide nanosheets supported bismuth tungsten oxide nanoflakes heterostructure as an efficient photocatalyst for the tetracycline degradation. Chemosphere 299,. https://doi.org/10.1016/j.chemosphere.2022.134477 134477.

Su, Y., Xu, X., Li, R., Luo, X., Yao, H., Fang, S., Peter Homewood, K., Huang, Z., Gao, Y., Chen, X., 2022. Design and fabrication of a CdS QDs/Bi_2WO_6 monolayer S-scheme heterojunction configuration for highly efficient photocatalytic degradation of trace ethylene in air. Chem. Eng. J. 429,. https://doi.org/10.1016/j.cej.2021.132241 132241.

Sun, H., Qin, P., Wu, Z., Liao, C., Guo, J., Luo, S., Chai, Y., 2020. Visible light-driven photocatalytic degradation of organic pollutants by a novel Ag_3VO_4/Ag_2CO_3 p–n heterojunction photocatalyst: Mechanistic insight and degradation pathways. J. Alloys Compd. 834,. https://doi.org/10.1016/j.jallcom.2020.155211 155211.

Tang, Q.Y., Yang, M.J., Yang, S.Y., Xu, Y.H., 2021. Enhanced photocatalytic degradation of glyphosate over 2D CoS/BiOBr heterojunctions under visible light irradiation. J. Hazard. Mater. 407,. https://doi.org/10.1016/j.jhazmat.2020.124798 124798.

Thangasamy, P., Maruthapandian, V., Saraswathy, V., Sathish, M., 2017. Supercritical fluid processing for the synthesis of NiS_2 nanostructures as efficient electrocatalysts for electrochemical oxygen evolution reactions. Catal. Sci. Technol. 7, 3591–3597. https://doi.org/10.1039/c7cy01103b.

Wang W, Zhao W, Zhang H, Dou X and H, S., 2021. 2D/2D step-scheme α-Fe_2O_3/Bi_2WO_6 photocatalyst with efficient charge transfer for enhanced photo-Fenton catalytic activity. Chin. J. Catal. 42, 97-106. Doi: 10.1016/S1872-2067(20)63602-6.

Wang, Z., Liang, X., Zhu, Y., Zouhu, X., Feng, X., Zhu, R., 2019. Ag and Cu_2O modified 3D flower-like ZnO nanocomposites and evaluated by photocatalysis oxidation activity regulation. Ceram. Int. 45, 23310–23319. https://doi.org/10.1016/j.ceramint.2019.08.030.

Wang, X., Xu, G., Tu, Y., Wu, D., Li, A., Xie, X., 2021. BiOBr/PBCD-B-D dual-function catalyst with oxygen vacancies for Acid Orange 7 removal: Evaluation of adsorption-photocatalysis performance and synergy mechanism. Chem. Eng. J. 411,. https://doi.org/10.1016/j.cej.2021.128456 128456.

Wiśniewska, M., Szyłak-Szydłowski, M., 2021. The air and sewage pollutants from biological waste treatment. Processes. 9, 250. https://doi.org/10.3390/pr9020250.

Wu, Y., Ji, H., Liu, Q., Sun, Z., Li, P., Ding, P., Guo, M., Yi, X., Xu, W., Wang, C.C., Gao, S., Wang, Q., Liu, W., Chen, S., 2022. Visible light photocatalytic degradation of sulfanilamide enhanced by Mo doping of BiOBr nanoflowers. J. Hazard. Mater. 424,. https://doi.org/10.1016/j.jhazmat.2021.127563 127563.

Xiao, H., Liu, R., Zhao, X., Qu, J., 2008. Enhanced degradation of 2,4-dinitrotoluene by ozonation in the presence of manganese(II) and oxalic acid. J. Mol. Catal. A: Chem. 286, 149–155. https://doi.org/10.1016/j.molcata.2008.02.013.

Xing, Y., Lu, X., Li, Y., Yang, B., Huang, Y., Zhang, M., Cheng, J., Min, X., Pan, W., 2022. Self-assembled $Ag_4V_2O_7$/Ag_3VO_4 Z-scheme heterojunction by pH adjustment with efficient photocatalytic performance. J. Adv. Ceram. 11, 1789–1800. https://doi.org/10.1007/s40145-022-0648-5.

Xu, F., Meng, K., Cheng, B., Wang, S., Xu, J., Yu, J., 2020. Unique S-scheme heterojunctions in self-assembled TiO_2/CsPbBr3 hybrids for CO_2 photoreduction. Nat. Commun. 11, 4613. https://doi.org/10.1038/s41467-020-18350-7.

Yang, H., Cao, R., Sun, P., Yin, J., Zhang, S., Xu, X., 2019. Constructing electrostatic self-assembled 2D/2D ultra-thin $ZnIn_2S_4$/protonated g-C_3N_4 heterojunctions for excellent photocatalytic performance under visible light. Appl. Catal. B: Environ. 256,. https://doi.org/10.1016/j.apcatb.2019.117862 117862.

Yang, J., Su, H., Wu, Y., Li, D., Zhang, D., Sun, H., Yin, S., 2021. Facile synthesis of kermesinus BiOI with oxygen vacancy for efficient hydrogen generation. Chem. Eng. J. 420,. https://doi.org/10.1016/j.cej.2020.127607 127607.

Yin, S., Sun, L., Zhou, Y., Li, X., Li, J., Song, X., Huo, P., Wang, H., Yan, Y., 2021. Enhanced electron–hole separation in SnS_2/Au/g-C_3N_4 embedded structure for efficient CO_2 photoreduction. Chem. Eng. J. 406,. https://doi.org/10.1016/j.cej.2020.126776 126776.

Yu, H., Huang, J., Jiang, L., Shi, Y., Yi, K., Zhang, W., Zhang, J., Chen, H., Yuan, X., 2020. Enhanced photocatalytic tetracycline degradation using N-CQDs/OV-BiOBr composites: Unraveling the complementary effects between N-CQDs and oxygen vacancy. Chem. Eng. J. 402,. https://doi.org/10.1016/j.cej.2020.126187 126187.

Yu, H., Huang, J., Jiang, L., Leng, L., Yi, K., Zhang, W., Zhang, C., Yuan, X., 2021. In situ construction of Sn-doped structurally compatible heterojunction with enhanced interfacial electric field for photocatalytic pollutants removal and CO_2 reduction. Appl. Catal. B: Environ. 298,. https://doi.org/10.1016/j.apcatb.2021.120618 120618.

Zai, J., Wei, X., Sun, M., Tian, H., Liu, X., Qi, R., Qian, X., 2021. Light absorption, photocarrier dynamic properties of hierarchical SnS_2 microspheres and their performances on photodegradation of high concentration Rhodamine B. J. Photoch. Photobio. A 415,. https://doi.org/10.1016/j.jphotochem.2021.113320 113320.

Zhang, R., Cai, L., Cai, Y., Han, Q., Li, Y., Zhang, T., Liu, Y., Zeng, K., Zhao, C., Yu, J., Yang, Z., 2021. Lamellar insert SnS_2 anchored on BiOBr for enhanced photocatalytic degradation of organic pollutant under visible-light. Colloid Surface A 618,. https://doi.org/10.1016/j.colsurfa.2021.126444 126444.

Zhang, B., Hu, X., Liu, E., Fan, J., 2021. Novel S-scheme 2D/2D BiOBr/g-C_3N_4 heterojunctions with enhanced photocatalytic activity. Chin. J. Catal. 42, 1519–1529. https://doi.org/10.1016/s1872-2067(20)63765-2.

Zhang, X., Huang, W., Xia, Z., Xian, M., Bu, F., Liang, F., Feng, D., 2022. One-pot synthesis of S-scheme WO_3/BiOBr heterojunction nanoflowers enriched with oxygen vacancies for enhanced tetracycline photodegradation. Sep. Purif. Technol. 290,. https://doi.org/10.1016/j.seppur.2022.120897 120897.

Zhang, C., Jia, M., Xu, Z., Xiong, W., Yang, Z., Cao, J., Peng, H., Xu, H., Xiang, Y., Jing, Y., 2022. Constructing 2D/2D N-ZnO/g-C_3N_4 S-scheme heterojunction: Efficient photocatalytic performance for norfloxacin degradation. Chem. Eng. J. 430,. https://doi.org/10.1016/j.cej.2021.132652 132652.

Zhang, T., Maihemllti, M., Okitsu, K., Talifur, D., Tursun, Y., Abulizi, A., 2021. In situ self-assembled S-scheme BiOBr/pCN hybrid with enhanced photocatalytic activity for organic pollutant degradation and CO_2 reduction. Appl. Surf. Sci. 556,. https://doi.org/10.1016/j.apsusc.2021.149828 149828.

Zhang, W., Peng, Y., Yang, Y., Zhang, L., Bian, Z., Wang, H., 2022. Bismuth-rich strategy intensifies the molecular oxygen activation and internal electrical field for the photocatalytic degradation of tetracycline hydrochloride. Chem. Eng. J. 430,. https://doi.org/10.1016/j.cej.2021.132963 132963.

Zhang, Y., Qiu, J., Zhu, B., Fedin, M.V., Cheng, B., Yu, J., Zhang, L., 2022. ZnO/COF S-scheme heterojunction for improved photocatalytic H_2O_2 production performance. Chem. Eng. J. 444,. https://doi.org/10.1016/j.cej.2022.136584 136584.

Zhang, F., Shen, L., Li, J., Zhang, Y., Wang, G., Zhu, A., 2021. Room temperature photocatalytic deposition of Au nanoparticles on SnS_2 nanoplates for enhanced photocatalysis. Powder Technol. 383, 371–380. https://doi.org/10.1016/j.powtec.2021.01.065.

Zhang, L., Yue, X., Liu, J., Feng, J., Zhang, X., Zhang, C., Li, R., Fan, C., 2020. Facile synthesis of Bi_5O_7Br/BiOBr 2D/3D heterojunction as efficient visible-light-driven photocatalyst for pharmaceutical organic degradation. Sep. Purif. Technol. 231,. https://doi.org/10.1016/j.seppur.2019.115917 115917.

Zhang, B., Zhang, M., Zhang, L., Bingham, P.A., Tanaka, M., Li, W., Kubuki, S., 2021. BiOBr/MoS_2 catalyst as heterogenous peroxymonosulfate activator toward organic pollutant removal: Energy band alignment and mechanism insight. J. Colloid Interf. Sci. 594, 635–649. https://doi.org/10.1016/j.jcis.2021.03.066.

Zhao, W., Li, Y., Zhao, P., Zhang, L., Dai, B., Huang, H., Zhou, J., Zhu, Y., Ma, K., Leung, D.Y.C., 2021. Insights into the photocatalysis mechanism of the novel 2D/3D Z-Scheme g-C_3N_4/SnS_2 heterojunction photocatalysts with excellent photocatalytic performances. J. Hazard. Mater. 402,. https://doi.org/10.1016/j.jhazmat.2020.123711 123711.

Zhao, W., Wang, W., Han, T., Wang, H., Zhang, H., Shi, H., 2021. Oxygen vacancies boosted charge separation towards enhanced photodegradation ability over 3D/2D Z-scheme $BiO_{1-X}Br/Fe_2O_3$ heterostructures. Sep. Purif. Technol. 269,. https://doi.org/10.1016/j.seppur.2021.118693 118693.

Zhao, W., Li, Y., Zhao, P., Zhang, L., Dai, B., Xu, J., Huang, H., He, Y., Leung, D.Y.C., 2021. Novel Z-scheme Ag-C_3N_4/SnS_2 plasmonic heterojunction photocatalyst for degradation of tetracycline and H_2 production. Chem. Eng. J. 405,. https://doi.org/10.1016/j.cej.2020.126555 126555.

Zheng, H., Zhang, S., Yuan, J., Qin, T., Li, T., Sun, Y., Liu, X., Wong, D.K.Y., 2022. Amplified detection signal at a photoelectrochemical aptasensor with a poly(diphenylbutadiene)-BiOBr heterojunction and Au-modified CeO_2 octahedrons. Biosens. Bioelectron. 197,. https://doi.org/10.1016/j.bios.2021.113742 113742.

Zhou C, Shi X, Li D, Song Q, Zhou Y, Jiang D and W, S., 2021. Oxygen vacancy engineering of $BiOBr/HNb_3O_8$ Z-scheme hybrid photocatalyst for boosting photocatalytic conversion of CO_2. J. Colloid Interf. Sci. 599, 245-254. Doi: 10.1016/j.jcis.2021.04.064.

Zhou, J., Zhang, Z., Kong, X., He, F., Zhao, R., Wu, R., Wei, T., Wang, L., Feng, J., 2020. A novel P-N heterojunction with staggered energy level based on $ZnFe_2O_4$ decorating SnS_2 nanosheet for efficient photocatalytic degradation. Appl. Surf. Sci. 510,. https://doi.org/10.1016/j.apsusc.2020.145442 145442.